

Super Electrolyte-Philic Boron Nitride Nanotube Membranes as Highly Robust Separators for Lithium Batteries

Xidong Duan (✉ xidongduan@hnu.edu.cn)

State Key Laboratory for Chemo/Biosensing and Chemometrics, College of Chemistry and Chemical Engineering, Hunan University, Changsha 410082, China

Xiaohua Shen

State Key Laboratory for Chemo/Biosensing and Chemometrics, College of Chemistry and Chemical Engineering, Hunan University, Changsha 410082, China

Jian Zhu

UCLA <https://orcid.org/0000-0001-9852-1645>

Liqiang Zhang

State Key Laboratory for Chemo/Biosensing and Chemometrics, College of Chemistry and Chemical Engineering, Hunan University, Changsha 410082, China

Bailing Li

State Key Laboratory for Chemo/Biosensing and Chemometrics, College of Chemistry and Chemical Engineering, Hunan University, Changsha 410082, China

Hongmei Zhang

State Key Laboratory for Chemo/Biosensing and Chemometrics, College of Chemistry and Chemical Engineering, Hunan University, Changsha 410082, China

Lei Wang

State Key Laboratory for Chemo/Biosensing and Chemometrics, College of Chemistry and Chemical Engineering, Hunan University, Changsha 410082, China

Research Article

Keywords: Nanotube Membranes, Separators, Lithium Batteries, super electrolyte-philic ceramic separators

Posted Date: September 10th, 2020

DOI: <https://doi.org/10.21203/rs.3.rs-73317/v1>

License:  This work is licensed under a Creative Commons Attribution 4.0 International License.

[Read Full License](#)

Abstract

The widespread deployment of lithium ion (Li^+) batteries with increasing energy density entails a worsening safety concern. Among many contributing factors, the typical polymer separators are plagued with poor thermal stability, limited mechanical strength and lower Li^+ transference number, and are prone to catastrophic failure when subjected to local thermal or mechanical stress (e.g., pierced by lithium dendrites). Herein, we report an all-inorganic nonwoven boron nitride nanotube membrane featuring exceptional chemical stability, thermal stability, fire resistance and mechanical flexibility. The resulting membranes show superior wettability to electrolyte to endow excellent Li^+ transport properties with the lowest ionic resistance and the highest Li^+ transference number (0.86) when compared with all commercial separators. They can thus function as highly robust separators for Li/Li symmetric cells with ultralow overpotential (8.5 mV) and exceptional reversibility for repeated lithium plating/stripping cycles for over 8000 hours, and for practical $\text{LiFePO}_4/\text{Li}$ cell with unusually high temperature stability. Our study defines a unique class of super electrolyte-philic ceramic separators with favorable mechanical strength, thermal stability and ion transfer properties for advanced lithium batteries.

Main Text

Lithium ion batteries (LIBs) are ubiquitously recognized as the dominant energy storage devices for electric vehicles, energy storage stations and various portable electronic devices^{1,2,3,4}. As considerable efforts are devoted to further boosting the energy density or power density of LIBs, the potential catastrophic failure and the associated safety hazards are becoming increasingly critical challenges⁵. The separators play a crucial role in preventing the anode and cathode from short circuiting inside the LIBs while ensuring efficient lithium ion (Li^+) transport across. The current separators are generally based on porous membrane of various polymer materials (polyethylene, PE; or polypropylene, PP), which, although successful for commercial batteries, often suffer from limited mechanical strength and thermal stability that could compromise the battery lifetime or limit the application conditions⁵. Additionally, such polymeric separators usually feature a low porosity (30-40%) and low lithium ion transference number (t_{Li^+}), which limit overall battery performance^{6,7,8}. For example, the poor ionic transport properties lead to strong concentration gradient/polarization under high rate operating conditions, which contribute to uncontrollable lithium dendrite growth during repeated charge/discharge cycles, leading to short cycle life and serious safety issues^{9,10}. For instance, internal short circuit^{9,10} could happen at a low temperature of $\sim 65^\circ\text{C}$ when cell is operated at a high current rate^{11,12}. Overall, such non-idealities promote side reactions, degrades electrolyte and releases considerable Joule heating that further compromise cycling durability of the batteries^{13,14,15}. More seriously, the shrinkage and melting of polymer separators under thermal stress could lead to fire or explosion, causing catastrophic failure⁶. Therefore, low ionic conductivity and poor thermal stability of the separators represent critical challenges for battery safety.

Extensive efforts have been made to improve the thermal stability and/or mechanical stability of the separators by coating surface of polyolefin separators with inorganic nanostructures (e.g., SiO_2 , Al_2O_3 , $\text{Al}(\text{OH})_3$, $\text{Mg}(\text{OH})_2$, Zeolite, ZrO_2 and TiO_2)^{16,17,18,19,20}, incorporating inorganic fillers (e.g., BN nanosheets or BN nanotubes) in polymer composites^{5,21}, or introducing fire-resistant moieties such as hydroxyapatite²², polyimide²³ and triphenyl phosphate²⁴ in the polymer backbones. These strategies can generally improve the ionic conductivity, reduce the local heat accumulation to prevent thermal runaway, while increasing the mechanical strength and fire resistance to mitigate the risk of catastrophic failure. Nonetheless, the overall robustness of these separators is fundamentally limited by the thermal stability and mechanical strength of the polymer matrix, and can still fail under large thermal gradients or extended high-temperature exposure. Additionally, these designs don't address the ionic transport limitations of typical polymer membranes^{25,26,27}.

Herein, we report a new design of all inorganic ceramic separators based nonwoven boron nitride nanotube membranes (BNNTMs). The BNNTMs feature exceptional mechanical flexibility and thermal stability to endure high mechanical or thermal stress, and at the same time exhibit superior electrolyte wettability, high ionic conductivity (2 mS cm^{-1}) and high Li^+ ion transference number (0.86) to effectively minimize concentration polarization and suppress Li dendrite formation. They can thus function as highly robust separators for Li/Li symmetric cells with ultralow overpotential (8.5 mV) and exceptional reversibility for repeated lithium plating/stripping cycles for over 8,000 hours. Integrating BNNTMs with typical cathode and anode results in full batteries that with greatly enhanced rate capability. Furthermore, benefiting from its high thermal stability, the full batteries with BNNTMs can function well at high temperature up to $120 \text{ }^\circ\text{C}$, opening a pathway to high-temperature batteries. Our study defines a unique class of super electrolyte-philic ceramic separators with favorable mechanical strength, thermal stability and ion transfer properties for advanced LIBs.

Fig. 1a and Supplementary Fig. 1 schematically illustrate the fabrication process of BNNTMs (See method for details on BN growth). First, an electrospinning process was used to produce polypropylene cyanide (PAN) template followed by a high temperature carbonization process to produce nonwoven carbon fibers mats (CNNT) with tunable porous structure. Next, a chemical vapor deposition (CVD) process was carried out to form BN layer on the surface of the carbon fibers. Lastly, the carbon fiber template was thermally etched to obtain BNNTMs. The template-synthesized BNNTMs clearly manifest typical interconnected anisotropic fiber structures (Fig. 1b). High resolution scanning electron microscopy (SEM), transmission electron microscope (TEM) images demonstrate that the fibers in the BNNTMs feature a hollow tubular structure with the wall thickness about 80 nm (Fig. 1c and d). The corresponding energy dispersive X-ray (EDX) elementary mapping reveals uniform distribution of boron (B) and nitrogen (N) elements, with a small amount of oxygen (O) elements attributed to contamination in air during etch processes (Fig. 1e). The mechanical robustness under stress and deformation is a critical attribute of an ideal separator, which should withstand stress induced by local electrode volume change or lithium dendrite piercing²⁸. To this end, the BNNTMs exhibit extraordinary mechanical flexibility and strength, and can be fully folded and unfolded without affecting the structural integrity (Fig. 1f-i).

To evaluate the potential of the BNNTMs as separators for practical LIBs, we compared a series of key structural and physical properties of the BNNTMs with commercial polypropylene (PP), cellulose fiber (CF), ceramic (Ce), Lauren (La) separators. A summary of various physical properties of these separators are shown in Supplementary Table S1. Highly open and interconnected architecture is favorable for electrolyte stockpile and Li⁺ diffusion, improving the rate capability and cycling stability of batteries²⁹. To further evaluate the porous structure of separators, we conducted Gurley value and porosity test. A low Gurley value indicates fast air penetration through large pores or well-interconnected pores³⁰. The BNNTMs (Supplementary Fig. 2) display a highest porosity (85%) and a lowest Gurley value (56 s) compared to CF (64.7%; 130 s); CE and La manifest porosities of 60.7% and 75.2%, and Gurley values of 257 s and 192 s, respectively.

The physical deformation (e.g., shrinkage) of the separators under thermal stress may lead to serious safety hazards^{31,32}. Therefore, the thermal dimensional stability of the separators is critical for safe LIBs and dictates the highest temperature that the LIBs can operate. We have compared the thermal stability and flammability of the BNNTMs with commercial polyolefin (PP, CF, Ce, La) separators. Fig. 2a shows the optical photographs of these different separators after thermal treatment at various temperatures from 100 to 800 °C in air for 30 min. Although all separators largely retain the original shape at 100 °C, the PP, Ce and La separators start to exhibit notable dimensional shrinkage and crispation at 150 °C and clearly decompose at 250 °C (color turns black). CF also deforms instantaneously at 250 °C and completely vaporizes at 300 °C. In contrast, the BNNTMs show extraordinary structure integrity up to 800 °C, which is important for retaining the safety of the failing LIBs in which the local joule heating can exceed 200 °C³³. The thermal stability of the separators at such high temperature can ensure structural integrity and prevent short circuiting, thermal runaway and catastrophic failure. Fig 2b compares the temperature at which large deformation occurs for each separator.

We have further conducted thermal gravity test and found that the BNNTMs show little weight loss up to 800 °C in air (Fig. 2b), confirming its excellent thermal stability. In contrast, all other commercial separators lost >70% of the total weight in the temperature regime of 300-400 °C, confirming serious chemical degradation at such temperature. Furthermore, the X-ray diffraction (XRD) analysis and Fourier transform infrared (FTIR) spectroscopy studies of the thermally stressed BNNTMs reveal that the major diffraction patterns and absorption peaks are well retained after thermal treatment (Supplementary Fig. 3), further demonstrating the intrinsic material stability of the BNNTMs.

We have further conducted flammability test. The PP and CF are immediately melted and burned out upon contacting with flame, and the Ce and La are also easily ignited and combusted (Supplementary Fig. 4). With extraordinary thermal stability and chemical inertness, the BNNTMs show no obvious structural change in flame, demonstrating outstanding incombustibility with significant potential as flame-resistant separators.

Change of pore size in commercial polyolefin separators under thermal stress may degrade the cycling performance or cause serious safety issues³⁴. The SEM images of the separators after annealing at 150

°C for 1 h are shown in Figure 2c-l. In general, the oriented elliptical pores notably shrink and turn to round in PP separator due softening and shrinking of PP under thermal stress. Similar pore shrinkages are also observed in for Ce and La membranes, whereas the CF and BNNTMs largely maintain homogeneous interconnected porous architecture.

Ion transport properties across the separators are mostly governed by the wettability of the electrolytes³⁵. The high electrolyte uptake ability of the separators is essential for high ionic conductivity³⁰. We have therefore evaluated electrolyte wetting behavior of different separators by conducting the contact angle measurements and evaluating the wetted area as a function of the contacting time (Fig. 3a). The wettability depends upon a number of factors, including intrinsic molecular interactions, porosity, and surface roughness. A small droplet of electrolyte on the PP separator shows little change after 60 s of contact, indicating a poor wettability, which can be attributed to the low surface energy and nonpolar nature of PP⁶. Ce and La exhibit better wettability than PP owing to their polar Al-OH groups of Al₂O₃ particles and polar -NH₂ groups of benzoyl diamine on the coating layer. The CF and BNNTMs demonstrate excellent affinity to the electrolytes. In particular, the electrolyte is instantly absorbed into BNNTMs upon in contact, which exhibits essentially zero degree of contact angle (Fig. 3b and Supplementary Fig. 5), suggesting super electrolyte-philic nature of the BNNTMs. The BNNTMs show the highest uptake ability (548%) compared with commercial separators (PP: 40%, CF: 98%, Ce: 85%, La: 106%) after the immersion in the liquid electrolyte for 3 h. The excellent wettability and electrolyte uptake characters may be attributed to the polar B-N bonds that have favorable interaction with the electrolyte (to be further discussed later) and the 3D interwoven porous architectures that further enhance the wettability endow super electrolyte-philic characteristics^{36,37}. Such a superior wettability promises high ion conductivity to ensure the uniformity of Li ion flux and mitigates uneven Li ion transport, deposition and filament formation.

We have next evaluated the ion transport properties across the BNNTMs by conducting electrochemical impedance spectroscopy (EIS) studies. Expectedly, the BNNTMs show the highest ionic conductivity (2.00 mS cm⁻¹) at 25 °C (Fig. 3c and Supplementary Fig. 6), which is about 7.2, 1.5, 3.9 and 2.1 times of those of PP (0.28 mS cm⁻¹), CF (1.33 mS cm⁻¹), Ce (0.51 mS cm⁻¹), La (0.95 mS cm⁻¹). Fig. 3d shows Nyquist plots for BNNTMs at different temperature and the corresponding impedance values (horizontal X-axis intersects) (see the Supplementary Fig. 7 for Nyquist plots and corresponding impedance values for commercial separators). Fig. 3e exhibits corresponding Arrhenius plots of ionic conductivity (σ) and Linear fitting results for different separators. It is clear that the ionic conductivity of the BNNTMs is higher at all temperature. Additionally, the BNNTMs show the lowest activation energy (E_a) of 0.08 eV for ion transport, compared to 0.10-0.28 eV for other separators (Fig. 3f), which is expected to reduce the Ohmic polarization and therefore enhance the electrochemical performance of batteries.

Lithium-ion transference number (t_{Li^+}) is a critical parameter when evaluating the ionic conductivity for Li-ion batteries. Low t_{Li^+} gives rise to concentration polarization, leading to side reactions, dendrite growth and joule heating, which can shorten cycling life and cause catastrophic failure especially under fast

charging/discharging condition^{38,39}. It is thus important to determine the extract t_{Li^+} . Our measurements give a t_{Li^+} of 0.86 for the BNNTMs, which is considerably higher than those of the other commercial separators (0.37-0.69) (Fig. 3g, h and Supplementary Fig. 8). The simulated equivalent circuit and the AC impedance spectra results of symmetrical battery are shown in Supplementary Table S2.

Such improvement could be interpreted from two aspects. On one hand, the BNNTMs own high porosity, excellent wettability and uptake to the liquid electrolyte. On the other hand, BN may act as both a Lewis base and acid. Li ions may directly interact with nitrogen (Lewis base) in BN instead of intensely solvated by solvent molecules before deposition, and thus speed up the dissociation of Li ions and lithium salt. X-ray photoelectron spectroscopy (XPS) was performed to investigate interactions of the BNNTMs toward Li ions. After electrolyte absorbing, an additional peak at 402.9 eV is emerged in N 1s, and the Li 1s shows an obvious peak splitting (55.6 eV) (Figure 3i-j), which are ascribed to the newly formed Li-N bonds⁴⁰. B-species of BN can work as Lewis acid to trap the anions of the electrolyte and thus dissociate them from the Li⁺-coordinated anion state. To confirm this assumption, the BNNTMs were immersed in electrolyte and dried overnight. Raman spectroscopy was then performed to investigate the interaction between B and anion (PF₆⁻). The electrolyte exhibits characteristic Raman peaks of 901, 745, 722 and 525 cm⁻¹ (Figure 3k and Supplementary Fig. 9). The BNNTMs show no peaks in the region of 100-1000 cm⁻¹. Whereas, after absorbing electrolyte, the BNNTMs show resonance peaks with different positions and intensities from those of the electrolyte itself, indicating strong interactions between the BNNTMs and the electrolyte. To further confirm anion-trapping ability of the BNNTMs, TFSI⁻ vibration was monitored to analyzing the Li⁺ coordination state with TFSI⁻ anion. It could be divided into two components: free TFSI⁻ (742 cm⁻¹) and Li⁺ coordinated TFSI⁻ anions (748 cm⁻¹)⁴¹. Supplementary Fig. 10 clearly shows that BNNTMs demonstrate a larger content of dissociated Li⁺ ions through immobilization of TFSI⁻ anion than other separators. Therefore, the BNNTMs exhibit much improved t_{Li^+} . Being both a Lewis acid and base, the BNNTMs show favorable interaction with both the cations and anions, leading to superior wettability, and combining its highly porous structure, the BNNTMs show much desired super electrolyte philicity.

Lastly, we have further evaluated the enhanced electrochemical stability of the BNNTMs by conducting linear sweep voltammetry (LSV) (Fig. 3l). In general, with the commercial separators, the LSV show a notable current density increases at potentials above 4.3 V, indicating the onset of electrolyte decomposition. Significantly, no current increase is observed with the BNNTMs until a much higher potential of ~5.3 V, suggesting a much higher decomposition potential and wider electrochemical window. The improved stability is an interesting topic for further studies, which might be partly attributed to the strong interactions between the BN with anions, which may help lower the extent of anion oxidation at a high potential^{42,43}, thus alleviating the decomposition of the carbonate electrolytes and promoting the kinetics of electrode reactions, generating a more stable interface between the electrolyte and the electrode. The wider electrochemical stable window would open opportunities for high-voltage LIBs.

The formation of Li dendrites during repeated cycling is a common challenge in lithium metal batteries. Such dendrite formation can be largely attributed to inefficient Li^+ transport that leads to concentration polarization and uneven charge distribution³⁸. It is important in controlling Li dendrite formation by alleviating the anion depletion-induced large electric fields near the Li anode. Based on their excellent electrolyte wettability and Li^+ transport properties, we have explored the BNNTMs as the separators for Li metal electrodes. Fig. 4a shows the cycle performance and voltage hysteresis of the Li symmetric cells at a current density of 1 mA cm^{-2} . With the BNNTMs as the separator, the galvanostatic plating/stripping profile shows highly stable electrochemical process with little potential undulation. In contrast, the overpotential gradually increases upon cycling for CF, and violently fluctuates after 230 h, which may be largely attributed Li dendrite growth/dissolve resulted from poor Li^+ transport and concentration polarization. Other commercial separators (PP, Ce, La) show similar cycle performance as the CF at the beginning, The PP stopped functioning at 150 h and the device with Ce and La separator fails within 400 h, indicating internal short-circuit of the cell, probably owing to Li dendrite piercing separator. The magnified profiles of different cycles for the BNNTMs display a flat voltage plateau throughout the testing period, while the commercial separators show rather different arc-like profiles with pronounced voltage variation. The overpotentials for commercial separators (PP, CF, Ce and La) at 100th cycle are 75 mV, 9 mV, 45 mV, 41 mV, respectively (Supplementary Fig. 11). In contrast, the device with BNNTMs shows stable voltage profiles with an ultra-small overpotential (8.5 mV) beyond 6,500 h, which remains $\sim 20 \text{ mV}$ after 8,000 h continuous operation.

When the high current density of 3.5 mA cm^{-2} is applied, concentration polarization starts to increase. Uneven current distribution and Li deposition may result in increasing overpotential during cycles. For example, the commercial separators show a much large overpotential up to $\sim 500 \text{ mV}$ with large voltage fluctuations. Nonetheless, the device with the BNNTMs still exhibits outstanding stability for more than 700 h with a stable overpotential of 12 mV (Fig. 4b, and inset)).

We have further compared the photographs and SEM images of fresh Li foil and Li electrode after 340 mAh cm^{-2} cumulative capacity at 1 mA cm^{-2} to evaluate the lithium metal surface morphology change over cycling (Fig. 4c-h and Supplementary Fig. 12). Before cycling, the fresh Li foil exhibits metal luster with relatively flat surface. After cycling with different commercial separators, the Li foils show apparent blackening trend. By contrast, the metal luster is largely retained in Li foil cycled with BNNTMs. The SEM images of the fresh Li foil show relatively flat surface, while those of Li foils cycled with commercial separators show considerable surface roughness and inhomogeneity due to Li dendrite formation. On the other hand, the SEM image of Li foil cycled with BNNTMs show relatively smooth surface largely comparable to the fresh foil, indicating little dendrite formation. Significantly, the metal luster and relatively smooth surface are also largely retained in device with BNNTMs after cycling at 3.5 mA cm^{-2} (Fig. 4i), demonstrating little dendrite formation even under high current density.

The long-term stability and well-controlled Li deposition endowed by BNNTMs are originated from the collective effect of its favorable interactions with electrolyte to unify Li^+ flux. As compared with results

across the published reports, the devices with the BNNTMs separator exhibit excellent Li dendrite-suppressing ability to enable exceptional small overpotential (Supplementary Fig. 13) and cycling stability with a cumulative lifetime capacity exceeding $4,000 \text{ mAh cm}^{-2}$, exceeding the lifetime capacity of typical LIBs (typically $< 2,000 \text{ mAh cm}^{-2}$)^{44,45,46,47,48,49,50,51,52,53,54,55,56,57,58,59,60} (Fig. 4j) (Details are shown in Supplementary Table S3). Such excellent performances may be largely attributed to excellent electrolyte wettability, high ionic conductivity and high Li^+ transference number of the BNNTMs separator, which contribute to efficient Li^+ transport and reduce Li^+ concentration polarization to ensure uniform Li deposition^{61,62,63,64}.

To assess the practical applicability of the BNNTMs in LIBs, we have also used the BNNTMs separators for $\text{LiNi}_{0.5}\text{Co}_{0.2}\text{Mn}_{0.3}\text{O}_2$ (NCM523)/graphite coin cells and compared the electrochemical performance of the same cells with commercial separators. Stepped rate performance tests were carried out from 0.1 to 5 C and then back to 1 C. Fig. 5a shows charge-discharge voltage profiles of 1st cycle for NCM/graphite cells. Supplementary Fig. 14 displays the typical charge-discharge voltage profiles of full cells at different rates. Overall, the cell with BNNTMs delivers much better rate capability and manifests discharge capacities of 308.7, 278.8, 259.7, 215.5, 185.9, 136.8 and 97.8 mAh g^{-1} at various rates 0.1 C, 0.5 C, 1 C, 2 C, 3 C, 4 C and 5 C, respectively (Fig. 5b). In contrast, the device with commercial separators (PP, Ce, La) fails to deliver meaningful capacity at 3 C.

To further verify the excellent thermal stability of the BNNTMs separators, we evaluated the cycling performance of $\text{LiFePO}_4/\text{Li}$ cell with various separators at 1 C by using commercial liquid electrolyte (LX-0081) at 120 °C. Clearly, The $\text{LiFePO}_4/\text{BNNTM}/\text{Li}$ cell shows stable voltage profiles and a gravimetric discharge capacity of 151.8 mAh g^{-1} with a CE of 99.99% at 120 °C (Figure 5c) and exhibits a relatively high gravimetric discharge capacity retention of 83%, while the cells with commercial separators stop running after several cycles (Supplementary Fig. 15). These results indicate that the BNNTMs separators can offer significant potentials for high temperature LIBs. It should also be noted that 120 °C operating temperature demonstrated here is not limited by the BNNTMs separators, but by the electrode materials or electrolyte used.

In summary, we have reported a unique design of all-inorganic BNNTMs separators with exceptional chemical stability, thermal stability, fire resistance and mechanical flexibility. The BNNTMs feature super electrolyte philicity to endow excellent Li^+ transport properties with the lowest ionic resistance and the highest Li^+ transference number compared with all commercial separators, making them highly robust separators for Li metal battery. Moreover, the BNNTMs separators exhibit better rate and cycling durability at room and 120 °C. Our study defines a unique class of super electrolyte-philic ceramic separators for advanced LIBs.

Declarations

Acknowledgements

Contributions

Competing interests The authors declare no competing financial interests.

Additional information

Correspondence and requests for materials

Reprints and permissions information is available at www.nature.com/reprints.

Publisher's note: Springer Nature remains neutral with regard to jurisdictional claims in published maps and institutional affiliations.

References

1. Zhang, C. et al., Anion-Sorbent Composite Separators for High-Rate Lithium-Ion Batteries. *Adv. Mater.* **31**, 1-8 (2019).
2. Waqas, M. et al., Recent Development in Separators for High-Temperature Lithium-Ion Batteries. *Small* **15**, 1-44 (2019).
3. Zhang, T. W. et al., Prawn Shell Derived Chitin Nanofiber Membranes as Advanced Sustainable Separators for Li/Na-Ion Batteries. *Nano Lett.* **17**, 4894-4901 (2017).
4. Zhang, J. T. et al., Designed Formation of Double-Shelled Ni-Fe Layered-Double-Hydroxide Nanocages for Efficient Oxygen Evolution Reaction. *Adv. Mater.* **32**, 1906432 (2020).
5. Rahman, M. M. et al., High temperature and high rate lithium-ion batteries with boron nitride nanotubes coated polypropylene separators. *Energy Storage Mater.* **19**, 352-359 (2019).
6. Zhang, T. W. et al., Sustainable Separators for High-Performance Lithium Ion Batteries Enabled by Chemical Modifications. *Adv. Funct. Mater.* **29**, 1-9 (2019).
7. Song, Q. Q. et al., Thermally stable, nano-porous and eco-friendly sodium alginate/attapulgite separator for lithium-ion batteries. *Energy Storage Mater.* **22**, 48-56 (2019).
8. Kim, J. H., Kim, J. H., Kim, J. M., Lee, Y. G., Lee, S. Y., Superlattice Crystals-Mimic, Flexible/Functional Ceramic Membranes: Beyond Polymeric Battery Separators. *Adv. Energy Mater.* **5**, 1-8 (2015).
9. Cheng, X. B. et al., Nanodiamonds suppress the growth of lithium dendrites. *Nat. Commun.* **8**, 2017.
10. Wu, Z. S., Ren, W. C., Xu, L., Li, F., Cheng, H. M., Doped Graphene Sheets As Anode Materials with Superhigh Rate and Large Capacity for Lithium Ion Batteries. *ACS Nano* **5**, 5463-5471 (2011).
11. Lee, H., Alcoutlabi, M., Watson, J. V., Zhang, X. W., Electrospun Nanofiber-Coated Separator Membranes for Lithium-Ion Rechargeable Batteries. *J. Appl. Polym. Sci.* **129**, 1939-1951 (2013).
12. Jeong, H. S., Kim, J. H., Lee, S. Y., A novel poly(vinylidene fluoride-hexafluoropropylene)/poly(ethylene terephthalate) composite nonwoven separator with phase inversion-controlled microporous structure for a lithium-ion battery. *J. Mater. Chem.* **20**, 9180-9186 (2010).

13. Yan, J. H. et al., Polymer Template Synthesis of Soft, Light, and Robust Oxide Ceramic Films. *iScience* **15**, 185-195 (2019).
14. Liu, X. et al., Thermal Runaway of Lithium-Ion Batteries without Internal Short Circuit. *Joule* **2**, 2047-2064 (2018).
15. Bai, P. et al., Interactions between Lithium Growths and Nanoporous Ceramic Separators. *Joule* **2**, 2434-2449 (2018).
16. Li, C. F. et al., Two-dimensional molecular brush-functionalized porous bilayer composite separators toward ultrastable high-current density lithium metal anodes. *Nat. Commun.* **10**, 1363-1372 (2019).
17. Xu, D. et al., In Situ Generated Fireproof Gel Polymer Electrolyte with $\text{Li}_{6.4}\text{Ga}_{0.2}\text{La}_3\text{Zr}_2\text{O}_{12}$ As Initiator and Ion-Conductive Filler. *Adv. Energy Mater.* (2019).
18. Jung, Y. S. et al., Improved Functionality of Lithium-Ion Batteries Enabled by Atomic Layer Deposition on the Porous Microstructure of Polymer Separators and Coating Electrodes. *Adv. Energy Mater.* **2**, 1022-1027 (2012).
19. Lei, D. N., Benson, J., Magasinski, A., Berdichevsky, G., Yushin, G., Transformation of bulk alloys to oxide nanowires. *Science* **355**, 267-271 (2017).
20. Xu, X. et al., Double-negative-index ceramic aerogels for thermal superinsulation. *Science* **363**, (2019).
21. Chhowalla, M., Jariwala, D., Hyperbolic 3D architectures with 2D ceramics. *Science* **363**, 6428 (2019).
22. Li, H. et al., High-Wettability and Fire-Resistant Separators Based on Hydroxyapatite Nanowires for Advanced Lithium-Ion Batteries. *Adv. Mater.* **29**, 1-11 (2017).
23. Zhang, B. et al., A superior thermostable and nonflammable composite membrane towards high power battery separator. *Nano Energy* **10**, 277-287 (2014).
24. Liu, K. et al., Electrospun core-shell microfiber separator with thermal-triggered flame-retardant properties for lithium-ion batteries. *Sci. Adv.* **3**, (2017).
25. Mao, X. F. et al., Polyethylene separator activated by hybrid coating improving Li^+ ion transference number and ionic conductivity for Li-metal battery. *J. Power Sources* **342**, 816-824 (2017).
26. Chi, M. M. et al., Excellent rate capability and cycle life of Li metal batteries with ZrO_2/POSS multilayer-assembled PE separators. *Nano Energy* **28**, 1-11 (2016).
27. Xu, W. X. et al., Layer-by-Layer Deposition of Organic-Inorganic Hybrid Multilayer on Microporous Polyethylene Separator to Enhance the Electrochemical Performance of Lithium-Ion Battery. *ACS Appl. Mater. Inter.* **7**, 20678-20686 (2015).
28. Kim, J. K. et al., Hierarchical Chitin Fibers with Aligned Nanofibrillar Architectures: A Nonwoven-Mat Separator for Lithium Metal Batteries. *ACS Nano* **11**, 6114-6121 (2017).
29. Wang, T. et al., Bacteria-Derived Biological Carbon Building Robust Li-S Batteries. *Nano Lett.* **19**, 4384-4390 (2019).
30. Shin, M. et al., Metamorphosis of Seaweeds into Multitalented Materials for Energy Storage Applications. *Adv. Energy Mater.* **9**, 1900570 (2019).

31. Dai, J. H. et al., A rational design of separator with substantially enhanced thermal features for lithium-ion batteries by the polydopamine-ceramic composite modification of polyolefin membranes. *Energy Environ. Sci.* **9**, 3252-3261 (2016).
32. Zhang, J. J. et al., Renewable and superior thermal-resistant cellulose-based composite nonwoven as lithium-ion battery separator. *ACS Appl. Mater. Inter.* **5**, 128-134 (2013).
33. Cheng, Q. et al., Stabilizing Solid Electrolyte-Anode Interface in Li-Metal Batteries by Boron Nitride-Based Nanocomposite Coating. *Joule* **3**, 1510-1522 (2019).
34. Xu, H. R. et al., Sandwich-like polythioetherimide-decorated polypropylene (Celgard2400) composite separators with heat resistance and wettability for safety lithium-ion batteries. *Int. J. Electrochem. Sci.* 788-802 (2020).
35. Kim, J.-H. et al., Functionalized Nanocellulose-Integrated Heterolayered Nanomats toward Smart Battery Separators. *Nano Lett.* **16**, 5533-5541 (2016).
36. Chen, L., Li, W., Fan, L. Z., Nan, C. W., Zhang, Q., Intercalated Electrolyte with High Transference Number for Dendrite-Free Solid-State Lithium Batteries. *Adv. Funct. Mater.* **29**, 1901047 (2019).
37. Kim, J. K. et al., Hierarchical Chitin Fibers with Aligned Nanofibrillar Architectures: A Nonwoven-Mat Separator for Lithium Metal Batteries. *ACS Nano* **11**, 6114-6121, (2017).
38. Yue, X. Y. et al., "Top-Down" Li Deposition Pathway Enabled by an Asymmetric Design for Li Composite Electrode. *Adv. Energy Mater.* **9**, (2019).
39. Guo, Y. P. et al., An Autotransferable g-C₃N₄ Li⁺-Modulating Layer toward Stable Lithium Anodes. *Adv. Mater.* **31**, (2019).
40. Yan, C. et al., Lithium Nitrate Solvation Chemistry in Carbonate Electrolyte Sustains High-Voltage Lithium Metal Batteries. *Angew. Chem. Int. Ed.* **57**, 14055-14059 (2018).
41. Kim, D. et al., Amine-Functionalized Boron Nitride Nanosheets: A New Functional Additive for Robust, Flexible Ion Gel Electrolyte with High Lithium-Ion Transference Number. *Adv. Funct. Mater.* **30**, 1910813 (2020).
42. Rodrigues, M. T. F. et al., Hexagonal Boron Nitride-Based Electrolyte Composite for Li-Ion Battery Operation from Room Temperature to 150 °C. *Adv. Energy Mater.* **6**, (2016).
43. Shim, J. et al., 2D boron nitride nanoflakes as a multifunctional additive in gel polymer electrolyte for safe, long cycle life and high rate lithium metal batteries. *Energy Environ. Sci.* **10**, 1911-1916 (2017).
44. Zhao, C. Z. et al., An ion redistributor for dendrite-free lithium metal anodes. *Sci. Adv.* **4**, 3446 (2018).
45. Pan, R. et al., Nanocellulose Modified Polyethylene Separators for Lithium Metal Batteries. *Small* **14**, 1704371 (2018).
46. Li, X. et al., A functional SrF₂ coated separator enabling a robust and dendrite-free solid electrolyte interphase on a lithium metal anode. *J. Mater. Chem. A* **7**, 21349-21361 (2019).
47. Li, C. F. et al., Two-dimensional molecular brush-functionalized porous bilayer composite separators toward ultrastable high-current density lithium metal anodes. *Nat. Commun.* **1**, 1 (2019).

48. Wang, W. et al., A 3D flexible and robust HAPs/PVA separator prepared by a freezing-drying method for safe lithium metal batteries. *J. Mater. Chem. A* **7**, 6859-6868 (2019).
49. Hu, Z. et al., Dendrite-Free Lithium Plating Induced by In Situ Transferring Protection Layer from Separator. *Adv. Funct. Mater.* **30**, 1907020 (2019).
50. Nie, L. et al., Biofilm Nanofiber-Coated Separators for Dendrite-Free Lithium Metal Anode and Ultrahigh-Rate Lithium Batteries. *ACS Appl. Mater. Inter.* **11**, 32373-32380 (2019).
51. Du, Q. C. et al., Bendable Network Built with Ultralong Silica Nanowires as a Stable Separator for High-Safety and High-Power Lithium-Metal Batteries. *ACS Appl. Mater. Inter.* **11**, 34895-34903 (2019).
52. Zhong, Y. et al., Metal Organic Framework Derivative Improving Lithium Metal Anode Cycling. *Adv. Funct. Mater.* **30**, 1907579 (2020).
53. Xiao, J. et al., In-Situ Formed Protecting Layer from Organic/Inorganic Concrete for Dendrite-Free Lithium Metal Anodes. *Nano Lett.* (2020).
54. Lei, Q. K. et al., Towards ultra-stable lithium metal batteries: Interfacial ionic flux regulated through LiAl LDH-modified polypropylene separator. *Chem. Eng. J.* **395**, 125187 (2020).
55. Wu, X. et al., Constructing multi-functional Janus separator toward highly stable lithium batteries. *Energy Storage Mater.* **28**, 153-159 (2020).
56. Yang, Y., Wang, W., Li, L., Li, B., Zhang, J., Stable cycling of Li-S batteries by simultaneously suppressing Li-dendrite growth and polysulfide shuttling enabled by a bioinspired separator. *J. Mater. Chem. A* **8**, 3692-3700 (2020).
57. Liang, J. et al., A Nano-shield Design for Separators to Resist Dendrite Formation in Lithium-Metal Batteries. *Angew. Chem. Int. Ed.* **59**, 6561-6566 (2020).
58. Yang, J. et al., Advanced nanoporous separators for stable lithium metal electrodeposition at ultrahigh current densities in liquid electrolytes. *J. Mater. Chem. A* **8**, 5095-5104 (2020).
59. Yan, J. et al., Realizing Dendrite-Free Lithium Deposition with a Composite Separator. *Nano Lett.* (2020).
60. Zou, P. et al., A Periodic "Self-Correction" Scheme for Synchronizing Lithium Plating/Stripping at Ultrahigh Cycling Capacity. *Adv. Funct. Mater.* **30**, 1910532 (2020).
61. Cheng, X. B. et al., Dendrite-Free Lithium Deposition Induced by Uniformly Distributed Lithium Ions for Efficient Lithium Metal Batteries. *Adv. Mater.* **28**, 2888-2895 (2016).
62. Liang, Z. et al., Polymer nanofiber-guided uniform lithium deposition for battery electrodes. *Nano Lett.* **15**, 2910-2916 (2015).
63. Zhang, R. et al., Lithiophilic Sites in Doped Graphene Guide Uniform Lithium Nucleation for Dendrite-Free Lithium Metal Anodes. *Angew. Chem. Int. Ed.* **56**, 7764 (2017).
64. Ryou, M. H. et al., Excellent Cycle Life of Lithium-Metal Anodes in Lithium-Ion Batteries with Mussel-Inspired Polydopamine-Coated Separators. *Adv. Energy Mater.* **2**, 645-650 (2012).
65. Pan, H., Cheng, Z. B., Chen, J. Q., Wang, R. H., Li, X. J., High sulfur content and volumetric capacity promised by a compact freestanding cathode for high-performance lithium-sulfur batteries. *Energy*

Storage Mater. (2019).

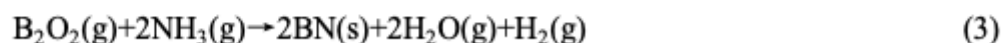
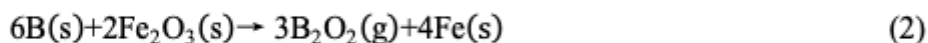
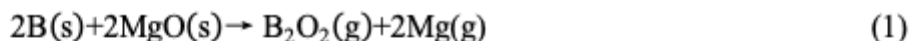
66. Chang, H. C., Tsai, H. J., Lin, W. Y., Chu, Y. C., Hsu, W. K., Hexagonal Boron Nitride Coated Carbon Nanotubes: Interlayer Polarization Improved Field Emission. *ACS Appl. Mater. Inter.* **7**, 14456-14462 (2015).
67. Chen, L. Y., Ye, H. H., Gogotsi, Y., Synthesis of Boron Nitride Coating on Carbon Nanotubes. *J. Am. Ceram. Soc.* **87**, 147-151 (2004).

Methods

Preparation of carbon fiber template. Polypropylene cyanide (PAN) template was first prepared by electrospinning process as previous report⁶⁵. Typically, PAN (1.2 g, Mw = 150000, Aldrich) was dissolved in N,N-dimethylformamide (DMF, 10 mL) and vigorously stirred at 75 °C for 12 h to form a homogeneous faint yellow solution. Then, the solution was loaded into a 12 mL syringe pump and spun at a flow rate of 1 mL h⁻¹ with a voltage of 18 kV. The fibers were peeled from collecting plate positioned at a distance of 15 cm from the nozzles and dried at 70 °C under vacuum overnight and further stabilized in air at 280 °C for 3 h. Then carbon fibers template (CNNTs) was obtained through that PAN fibers were anneal at 650 °C for 2 h at a ramp rate of 5 °C min⁻¹ under Ar atmosphere (30 sccm).

Preparation of BNNTMs separators. B powder, MgO, and γ-Fe₂O₃ with the molar ratio of 2:1:0.5 is mixed as precursors and were charged into bottom of a small one end closed quartz tube. The Carbon nanofiber template was placed upside of precursors. Subsequently, the tube was loaded into the furnace chamber. The precursor was heated to 1200 °C in 2 h with Ar as carrier (90 sccm) and then held for 120 min with 100 sccm NH₃ at this temperature. After reaction finished, it cooled down to room temperature under Ar protection. Then the BNNTMs separators were obtained using prepared BN/carbon template composites under burning at 700 °C in air for 2 h.

In the growth produces, the precursors produced B₂O₂ gas react with NH₃, resulting in the formation of BN on the surfaces of CNNTs^{66,67}. Once BN barrier layer on the surface of the CNNTs was completed, further reaction with the CNNTs is ceased. Corresponding chemical reactions are demonstrated as follows:



Other characterization techniques. The samples were characterized by scanning electron microscopy (SEM) images and electron dispersive X-ray spectroscopy (EDS) mappings of the samples were obtained on a SIGMA microscope (Zeiss, Germany) equipped with an EDS spectrometer. Transmission electron microscopy images and X-ray diffraction (XRD) patterns were obtained on a JEM-2100F microscope

(JEOL, Japan), a XRD-6100 spectrometer with Cu-K α radiation (Shimadzu, Japan). The thermotropic behavior was tested using Thermo Gravimetric Analyzer (TGA, model TGAQ 50, 30-800 °C, heating rate 10 °C min⁻¹ under air atmosphere), Fourier transform infrared spectra (FTIR) was obtained using IRTracer-100 (Shimadzu, Japan). The air permeability was tested using a Gurley-type densometer (BTY-B3P, Jinan Languang electromechanical technology co. LTD) by recording the time for 100 mL air passing through the separator (area = 1.21 cm²) under a given pressure. Electrolyte wetting behavior was conducted by dropping 5 μ l electrolyte (1 M LiPF₆ in EC/DMC (v:v=1:1) and 2% VC) onto each separator. The three-phase contact angle of separator was characterized by a JC2000C contact angle analyzer (Shanghai Zhongchen Digital Technology Equipment Co., Ltd., China). Raman spectra of blank BNNTMs and dried separators were performed using Raman spectroscopy (inVia Reflex, Renishaw with 488-nm laser as the excitation source). X-ray photoelectron spectroscopy (XPS) of BNNTMs and dried BNNTMs was obtained by X ray photoelectron spectrometer (AXIS SUPRA, Shimadzu-KRATOS, United Kingdom). Electrolyte (1 M LiPF₆ in EC/DMC (v:v=1:1) and 2% VC) was used for them. Raman spectra of TFSI⁻ vibration were monitored by soaking separators in electrolyte (1 M LiTFSI DOL/DME (v:v=1:1) and 2% LiNO₃) for 6 hours and then dried overnight. Electrochemical detection was obtained on an Autolab 302N electrochemical station (Metrohm, Switzerland).

Online Content Supplementary Information is available in the online version of the paper.

Data availability. The data that support the plots within this paper and other findings of this study are available from the corresponding author upon reasonable request.

Figures

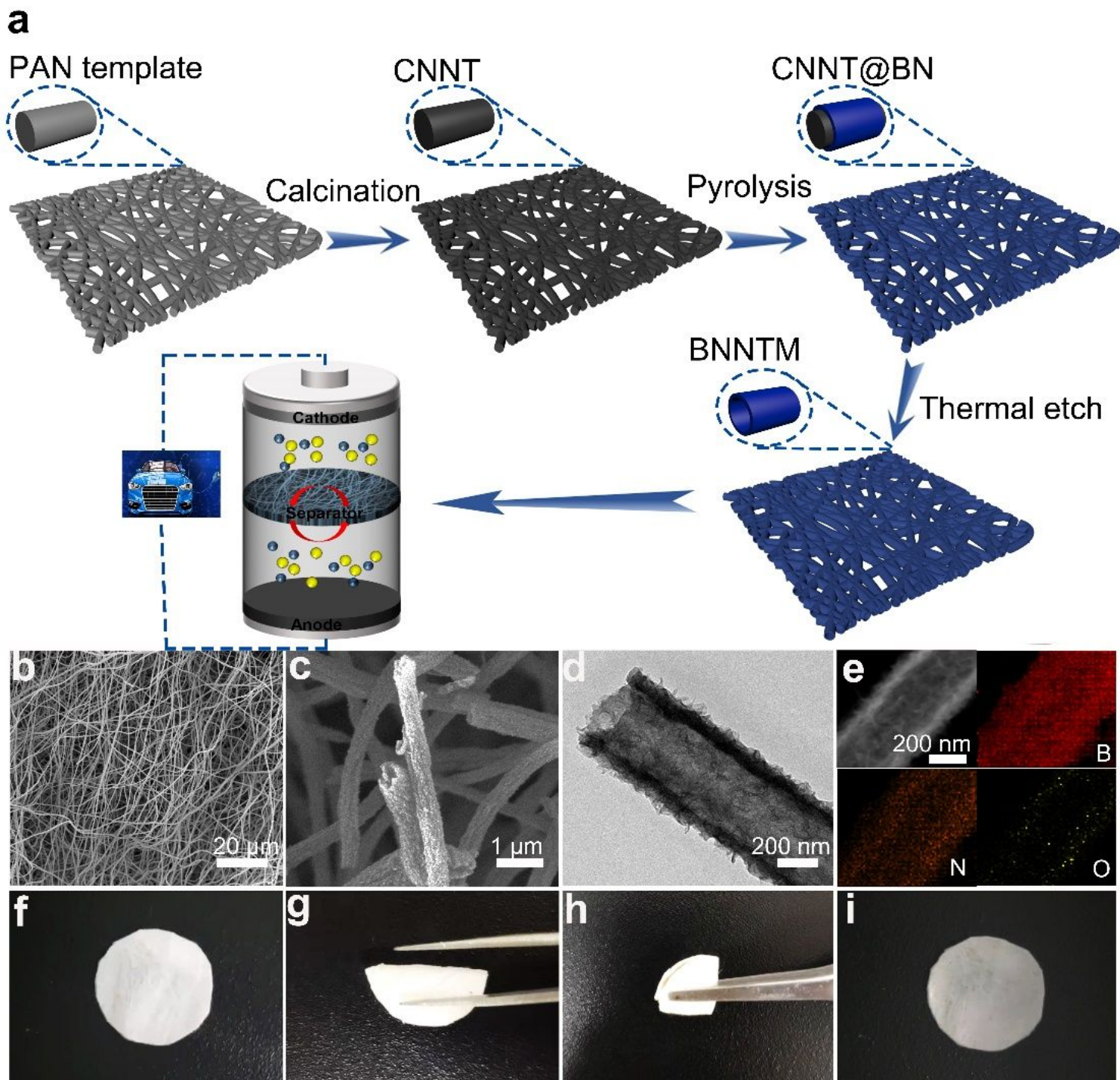


Figure 1

Fabrication process and morphology, composition, mechanical characterization of the BNNTMs. a, Schematic illustration of preparation procedures for BNNTMs (BN) by CVD method. b, c, the corresponding SEM images. d, TEM images of single BN nanotube. e, Elemental mapping images of BNNTMs. f-i, High flexibility of the BNNTMs under different bending conditions.

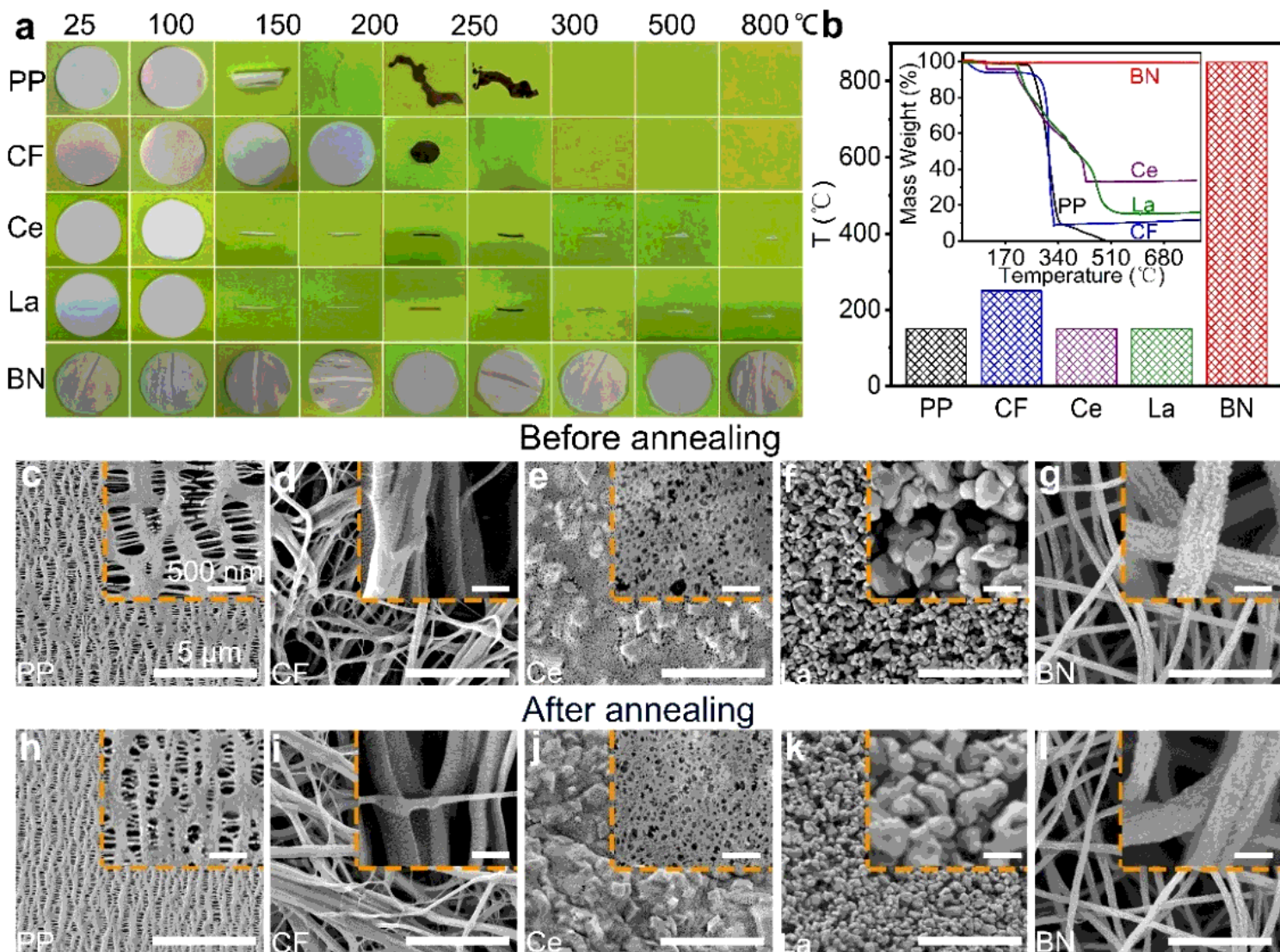


Figure 2

Thermal stability of BNNTMs. a, Optical photographs of separators (PP, CF, Ce, La and BNNTMs (BN)) before and after thermal treatment in tube furnace at different temperature for 0.5 hours. The one separator was used in entire execution process. b, The critical temperature at which large deformation occurs. Inside picture is Thermogravimetric test of different separators. c-l, SEM images of separators before and after thermal treatment in tube furnace at 150 °C for 1 hour. (c, h) PP, (d, i) CF, (e, j) Ce, (f, k) La, (g, l) BNNTMs (The scale bars are same as c).

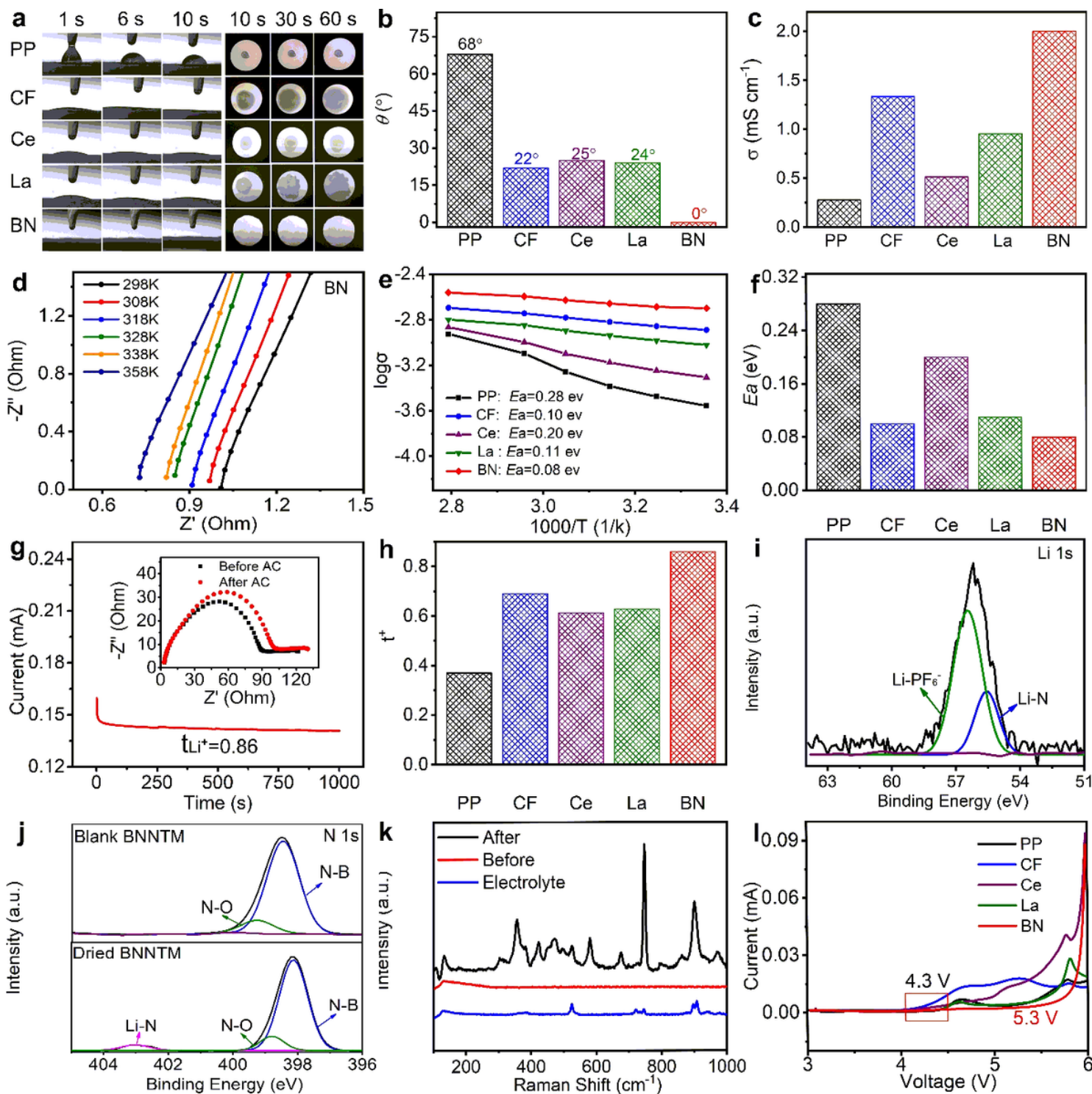


Figure 3

Properties characterization of different separators. a, Contact angles of electrolyte contacting on separators and time-resolved photograph of liquid electrolyte wettability test. b, Bar graph of corresponding contact angles. c, Calculated Ionic conductivity by Impedance spectra of the Stainless steel (SS)/Separator/SS cells in the frequency range from 0.1 Hz to 106 Hz with an amplitude of 10 mV. d, Nyquist Plot of BNNTMs at under different temperatures. e, Ionic conductivity and Arrhenius line fitting plots at different temperatures. f, Comparison of activation energy (E_a). g, Corresponding

chronoamperometry profile of BNNTMs under an initial bias voltage of 20 mV. The inset is EIS results of Li/Li symmetrical cells before and after chronoamperometry. h, Comparison of tLi+. i, j, XPS spectra of BNNTMs. N 1s (i), and Li 1s (j) high-resolution spectra. k, Raman spectra of BNNTMs before and after absorbing electrolyte (1 mol/L LiPF6 in 1:1 v/v EC/DMC with 2% VC) for 6 hours, and Raman spectra of electrolyte. l, Linear sweep voltammetry (LSV) (from 3 to 6 V) profiles of Li/SS cells at a scanning speed of 1 mV s⁻¹. The corresponding curves showing the electrochemical stability of the electrolyte with different separators at room temperature.

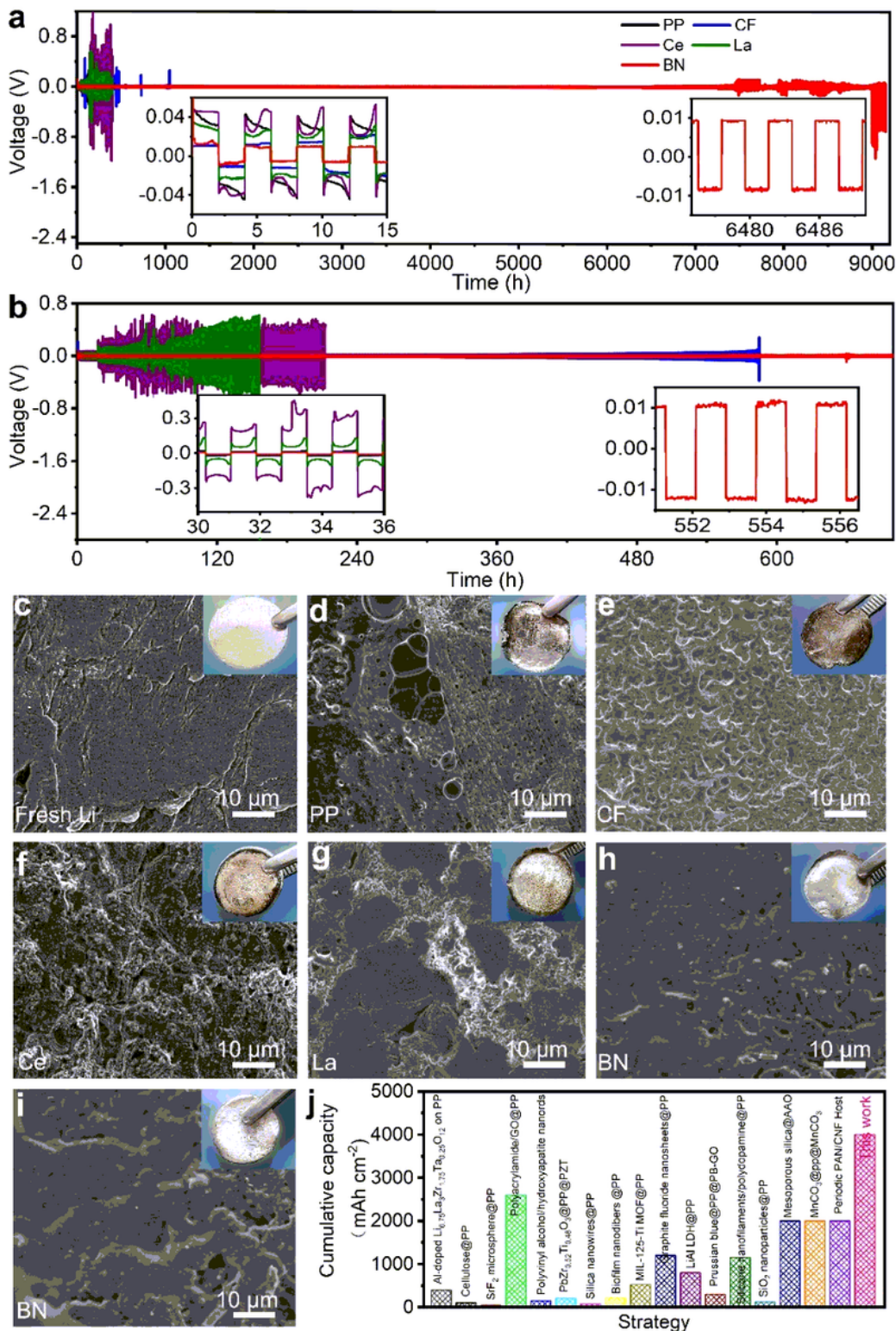
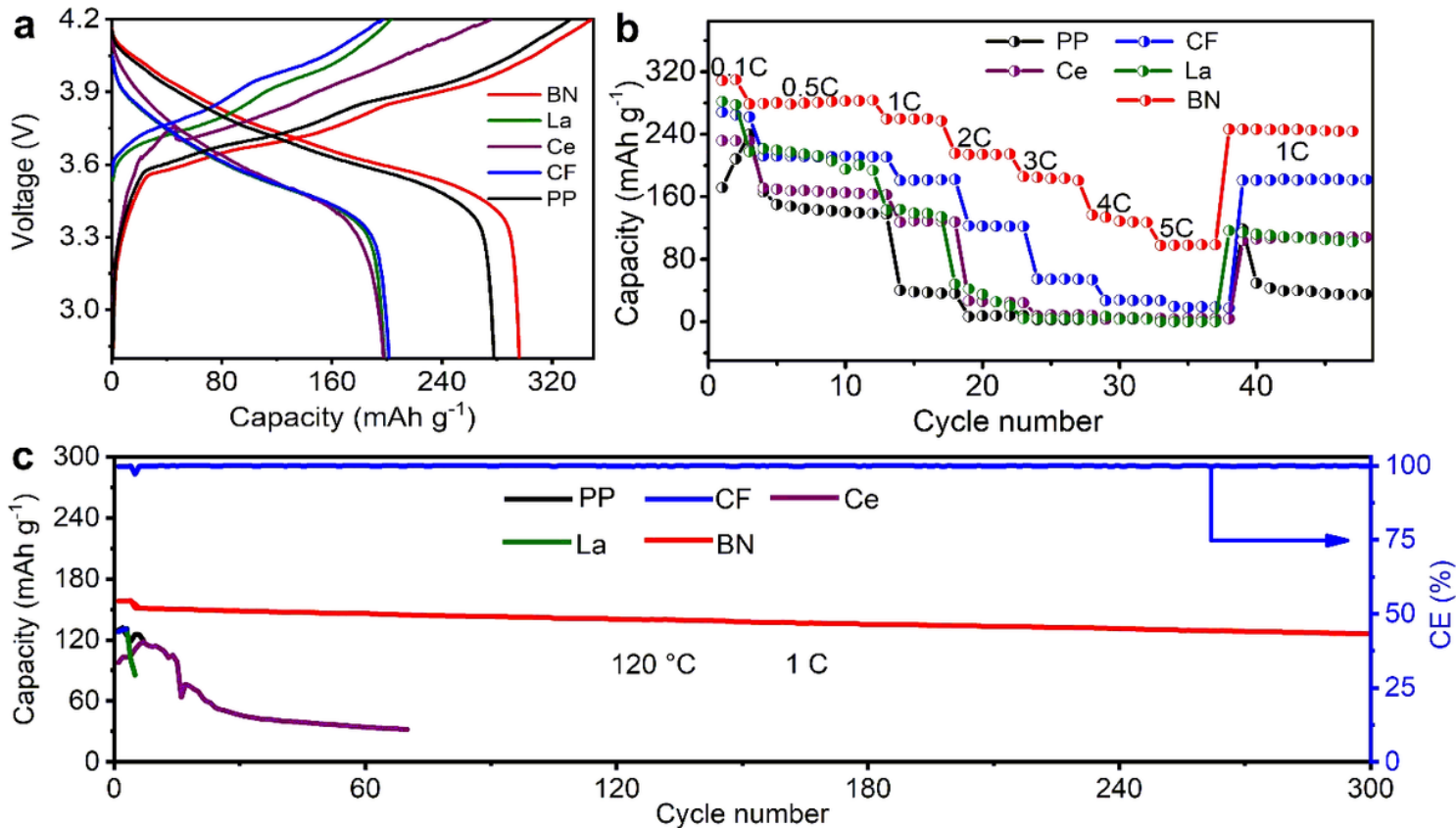


Figure 4

Lithium plating/stripping performance of BNNTMs separators. a, b, Galvanostatic plating/stripping profiles of Li / Li symmetric cells with different separators at low current density of 1 mA cm⁻² with 2 mAh cm⁻² cycling capacity (a) and at high current density of 3.5 mA cm⁻² with 2.8 mAh cm⁻² cycling capacity (b). The individual figures are stripping and plating curves at different states. c-i, The corresponding SEM of Li foil. Fresh (c) and after cycling 340 mAh cm⁻² cumulative capacity for different separators at 1 mA cm⁻² (d-h) and after 476 mAh cm⁻² cumulative capacity for BNNTMs at 3.5 mA cm⁻² (i), respectively. j, Comparison of plating/stripping cumulative capacity in Li/Li symmetric cells with existing papers.

**Figure 5**

Electrochemical performance of NCM/graphite full cells and LiFePO₄/Li cells using different separators. a, Corresponding galvanostatic charge-discharge voltage profiles for NCM/graphite full cells at 1 C (1st cycle). b, Rate performance of different separators for NCM/graphite full cells. c, Cycling performances of LiFePO₄/Li cell with BNNTMs at 1 C at 120 °C.